

FIG. 1.— Point spread function (PSF) decomposition for extracting spectra from our Keck/OSIRIS observations. *Left*: Examples of median-combined cubes for 2M0441+2301 Aab in *Jbb* (top row, blue), *Hbb* (middle row, green), and *Kbb* (bottom row, red) filters. The left panels show the data, the middle panels show our model fits composed of three bivariate Gaussians for each component, and the right panels show the residuals of the fits. The images are displayed with a logarithmic stretch and the DN represent median values across all spectral channels as opposed to the total flux at each pixel. The median rms of the residuals for all observations of the Aab pair are 0.13, 0.23, and 0.31 Data Numbers (DN) for *Jbb*, *Hbb*, and *Kbb*, respectively. For comparison, the average peak values of the median-collapsed cubes are 10.1, 23.8, and 24.8 DN. *Right*: Same as the left panels but for 2M0441+2301 Bab. The rms values for the Bab pair are 0.0056, 0.0097, and 0.012 DN for *Jbb*, *Hbb*, and *Kbb*. The average peak values are 0.14, 0.27, and 0.51 DN.

is dynamically stable. Both pairs are well-established members of Taurus (Luhman et al. 2009), have little or no reddening ($A_V \sim 0.2$ mag; Bulger et al. 2014), and are confirmed to be physical binaries rather than chance alignments based on multi-epoch astrometry (Todorov et al. 2014). An excess of mid-infrared emission was previously identified from both unresolved pairs, indicating that at least one component of each subsystem harbors a circum-(sub)stellar disk (Bulger et al. 2014; Adame et al. 2010). Spectroscopic validation is essential to confirm the low temperatures, luminosities, and masses of candidate planets at these very young ages when edge-on disks around brown dwarfs or low-mass stars can cause extinction and mimic the photometric properties of faint protoplanets (Kraus et al. 2014; Bowler et al. 2014; Wu et al. 2015).

Here, we present 1.2–2.4 μm spatially resolved imaging and spectroscopy of the four components of 2M0441+2301 AabBab. Our observations are described in Section 2; spectral classification, analysis of emission lines, and atmospheric model fits are detailed in Section 3; and we discuss the implications of our spectra in the context of planet formation models in Section 4.

2. OBSERVATIONS

We obtained moderate-resolution ($\lambda/\Delta\lambda \sim 3800$) integral field spectroscopy of 2M0441+2301 Aab and Bab with the OH-Suppressing Infrared Imaging Spectrograph (OSIRIS; Larkin et al. 2006) coupled with laser guide star adaptive optics (AO; Wizinowich et al. 2006; van Dam

et al. 2006) at the Keck I telescope on 2014 December 08 Universal Time (UT). OSIRIS samples over 1000 spectra in a single observation, resulting in a three-dimensional data cube with a field of view of $0''.32 \times 1''.28$ spanning about 1600 spectral channels for the $0''.020/\text{pixel}$ plate scale with broad band filters. Our observations benefited from the recently upgraded “G3” grating (Mieda et al. 2014).

2M0441+2301 Aa ($R = 14.2$ mag) was used as a reference tip tilt star for both binaries. The R -band magnitude of the laser guide star on the wavefront sensor remained steady at 9.3 mag during all the observations. Sky conditions were clear with excellent seeing between 0.4 – $0.6''$ in the optical as recorded by the Differential Image Motion Monitor at the Canada-France-Hawaii Telescope. We obtained a total of 40 min of on-source integration for 2M0441+2301 Aab in *Jbb* band (1.18–1.42 μm), 30 min in *Hbb* band (1.47–1.80 μm), and 30 min in *Kbb* band (1.97–2.38 μm) over an airmass of 1.0 to 1.2. For 2M0441+2301 Bab, we obtained 67 min in *Jbb*, 40 min in *Hbb*, and 40 min in *Kbb* spanning airmasses between 1.0–1.6 (Table 1). The instrument rotator was set to 90° for 2M0441+2301 Aab and 120° for Bab, and the observations were executed in an ABBA pattern with 0.4 – $0.5''$ dithers along the long axis of the reconstructed data cube. The A0V standard stars HD 19600 and HD 35036 were targeted immediately before and after both science objects with airmasses well matched to the associated science frames for each bandpass.

Basic image reduction including bad pixel removal, flat

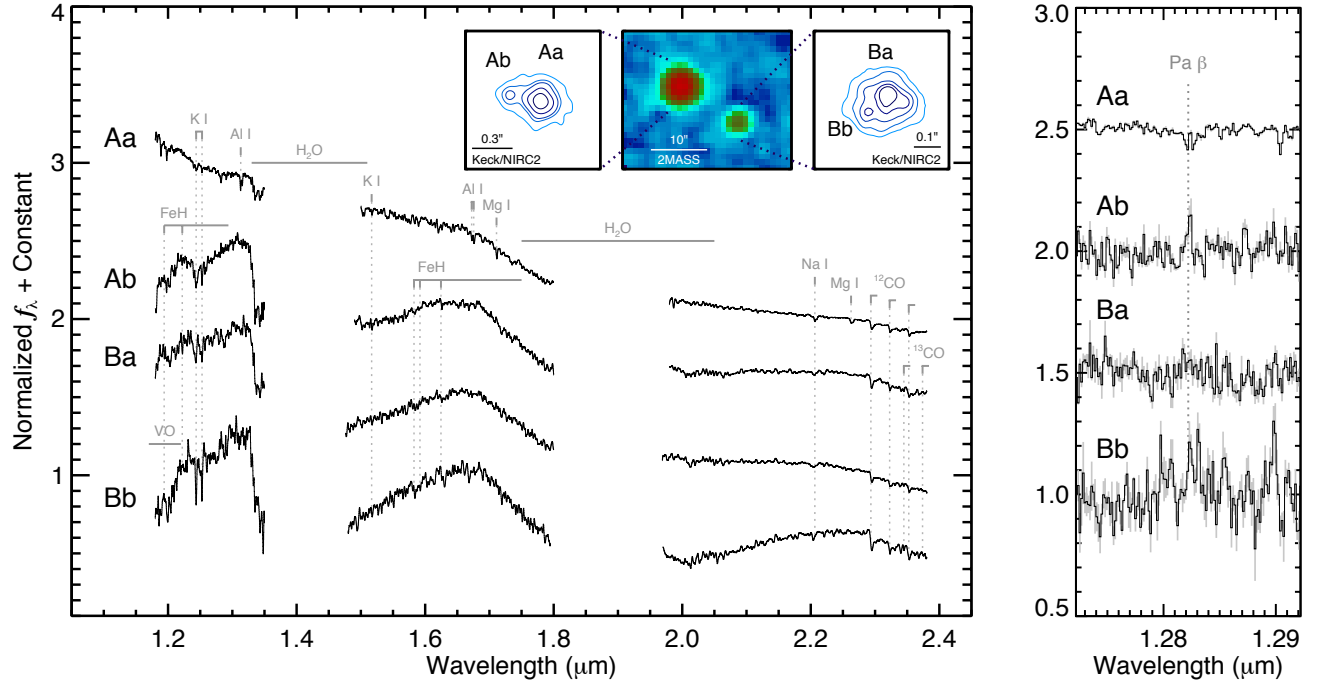


FIG. 2.— Near-infrared spectra of 2M0441+2301 Aa, Ab, Ba, and Bb. *Left*: Flux-calibrated 1.2–2.4 μm spectra. Major atomic and molecular features are labeled. The weak alkali lines such as K I at 1.25 μm and triangular *H*-band (1.5–1.8 μm) shapes in the substellar components are signatures of low surface gravities and extreme youth. The near-infrared spectral types based on the Allers & Liu (2013) classification scheme are $M7 \pm 1$, $M7 \pm 1$, and $L1 \pm 1$ for the Ab, Ba, and Bb components. All spectra have been smoothed from $R \sim 3800$ to $R \sim 1000$ for clarity, normalized, and offset by a constant. The inset shows the unresolved 2MASS K_S -band image of the system together with our AO images of each subsystem in K_S with NIRC2. Contours for the Aab pair represent 50%, 20%, 7%, 4%, and 1.5% of the peak flux. Contours for the Bab pair represent 50%, 33%, 20%, 10%, and 5% of the peak flux. Note that the Aab image has been convolved with a Gaussian for better rendering. *Right*: The Pa β spectral region at the native ($R \sim 3800$) resolving power. 2M0441+2301 Aa and Ab show weak but significant emission with equivalent widths of $-0.96 \pm 0.02 \text{ \AA}$ and $-0.84 \pm 0.11 \text{ \AA}$, respectively. The gray shaded region shows the 1σ flux density uncertainties.

fielding, pair-wise subtraction, wavelength calibration (in vacuum wavelengths), and assembly of the 2-D spectra into 3-D cubes was carried out using version 3.2 of the OSIRIS Data Reduction Pipeline with the most recent rectification matrices maintained by Keck Observatory. The current separation between 2M0441+2301Ba and Bb is 95 mas, which is only 1.8 diffraction limits at the 10-meter Keck telescope in *K* band. The fainter companions in each binary pair (Ab and Bb) are easily visible in all median-collapsed data cubes, but their PSFs overlap with those of their primaries, so robust spectral extraction free of systematics is not trivial. Our solution is to simultaneously fit analytical PSF models to each binary component by making use of the nonlinear least-squares curve fitting routine MPFIT (Markwardt 2009) written in Interactive Data Language (IDL). We tested four models for each binary component: a single bivariate Gaussian, a single Lorentzian, the sum of a bivariate Gaussian and Lorentzian, and the sum of three bivariate Gaussians. These increasingly complex models are designed to mimic the extended PSF halo and a more compact diffraction-limited core.

The PSFs of each component in our OSIRIS data have the same shape, remain at fixed relative positions in each cube, and both broaden in the same fashion at longer wavelengths, but their amplitudes vary with wavelength because of differing spectral slopes and absorption features. We therefore first fit each joint model to the binary in the median-combined cube to establish the posi-

tion of each model component, which is then held fixed for the PSF fit at each wavelength. All other parameters defining the PSF are allowed to vary, but the shape of each component (Aa and Ab, for example) is designed to remain mutually identical. Ultimately, we adopted the model composed of three Gaussians per binary component (i.e., six Gaussians per binary) because this produced the best fit as measured by the lowest residual rms. Fourteen free parameters define the Gaussian amplitudes, standard deviations, position angles, and overall offset of the binary model (Figure 1) and was used to fit our observations at each wavelength channel of every data cube and in all three filters for both 2M0441+2301 Aab and Bab. The same model (except for a single component instead of a binary) was used to extract the spectrum of the standard stars.

The extracted spectra are scaled to a common level and the mean and standard error at each wavelength are adopted as the flux density and its associated uncertainty. Telluric correction was carried out with the `xtellcor_general` routine in the IRTF/SpEx reduction package Spextool, which is written in IDL (Vacca et al. 2003; Cushing et al. 2004). Each band was independently flux calibrated by first converting unresolved 2MASS photometry of each subsystem into the OSIRIS filter system by deriving photometric transformations as a function of spectral type from synthetic photometry of MLT objects from the SpeX Prism Spectral Library (Burgasser 2014). Binary flux ratios are measured during the mod-

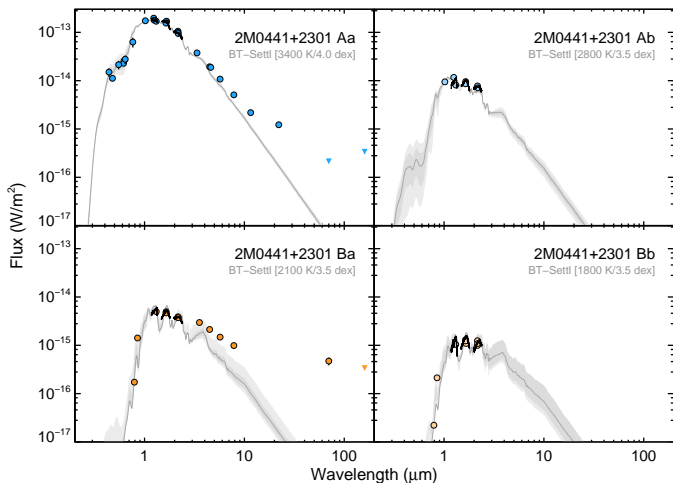


FIG. 3.— Spectral energy distributions for 2M0441+2301 Aab-Bab. Dark gray lines show the best matching BT-Settl models (as indicated in the legend) to $<3 \mu\text{m}$ photometry assuming $A_V=0.0$ mag, which avoids disk emission at longer wavelengths. Shaded regions show the 1σ and 2σ uncertainties. Photometry originates from the literature (Todorov et al. 2010; Bulger et al. 2014) and our own NIRC2 and OSIRIS observations. Unresolved excess emission from one or more subdisks is present beyond about $7 \mu\text{m}$ for the Aab component and $3 \mu\text{m}$ for Bab, shown here as associated with the primaries of each pair but which may also (or instead) originate from the companions. The flux-calibrated OSIRIS spectra are overplotted in black for comparison.

eling and spectral extraction of the science data and are used to calculate apparent magnitudes of each component in the OSIRIS filter system. Finally, a scale factor is derived to absolutely flux calibrate each bandpass of the spectrum to match the decomposed OSIRIS photometry (Figure 2). The signal-to-noise ratio per pixel is lower near the edges of each bandpass and is highest in the centers with median values across the entire $1.2\text{--}2.4 \mu\text{m}$ spectrum of 112 for Aa, 45 for Ab, 41 for Ba, and 24 for Bb.

In addition to our OSIRIS observations, we also obtained NIRC2 images of 2M0441+2301 AabBab at the Keck II telescope on 2014 November 10 UT using Natural Guide Star (NGS) AO. Sky conditions were clear with $0.5\text{--}0.6''$ seeing in the optical throughout the observations. We targeted the Aab component in Y , J (on the Mauna Kea Observatory, or MKO, filter system), H (MKO), and K_S filters and the Bab component in H (MKO), and K_S filters with the narrow camera mode, resulting in a field of view of $10''.2 \times 10''.2$. A plate scale of $9.952 \pm 0.002 \text{ mas pix}^{-1}$ and sky orientation on the detector of $0.252 \pm 0.009^\circ$ are adopted from Yelda et al. (2010). 2M0441+2301 Aa provided on-axis AO correction for the Aab pair, and we offset by $12''.3$ for off-axis imaging of the Bab components. The images were dark subtracted, flat fielded, and cleaned of cosmic rays and bad pixels. Relative photometry and astrometry was measured by fitting three bivariate Gaussians to each binary component in each image following Liu et al. (2010). We adopt the mean and standard deviation of these measurements, which are reported in Table 1.

3. RESULTS

3.1. Spectral Classification

The flux-calibrated spectra of 2M0441+2301 AabBab are shown in Figure 2. The substellar components Ab,

Ba, and Bb show strong atomic and molecular absorption features characteristic of young late-M to early-L type brown dwarfs with low surface gravities. These include shallow K I absorption lines at $1.25 \mu\text{m}$ and an angular spectral shape from 1.5 to $1.8 \mu\text{m}$ compared to old field objects (Allers & Liu 2013), which is primarily caused by weakened collision-induced absorption of molecular hydrogen at lower photospheric pressures (Marley et al. 2012; Barman et al. 2011). 2M0441+2301 Bb shows particularly pronounced features from water, carbon monoxide, iron hydride, and vanadium oxide. Index-based classification of the substellar components (Allers & Liu 2013) gives near-infrared spectral types of $M7 \pm 1$, $M7 \pm 1$, and $L1 \pm 1$ for 2M0441+2301 Ab, Ba, and Bb. We measure $1.2437 \mu\text{m}$ and $1.2529 \mu\text{m}$ K I equivalent widths of $3.5 \pm 0.3 \text{ \AA}$ and $0.0 \pm 0.3 \text{ \AA}$ for Ab; $2.3 \pm 0.3 \text{ \AA}$ and $0.8 \pm 0.5 \text{ \AA}$ for Ba; and $3.4 \pm 0.6 \text{ \AA}$ and $5.5 \pm 1.0 \text{ \AA}$ for Bb, respectively. Aa and Ba have very low gravity (“VL-G”) classifications, while Bb has an intermediate-gravity classification (“INT-G”).

3.2. Emission Lines and Accretion

2M0441+2301 Aa and Ab show weak $\text{Pa}\beta$ emission indicating ongoing accretion from subdisks around both binary components. No significant $\text{Pa}\beta$ emission is evident in 2M0441+2301 Ba or Bb, and there is no $\text{Br}\gamma$ emission in any components. The emission line from the primary is superimposed on a slightly broader absorption trough from unresolved Ti I, Fe I, and Ca I absorption lines (Rayner et al. 2009). We therefore define a pseudo-continuum level at $1.25 \pm 0.01 \times 10^{-13} \text{ W m}^{-2} \mu\text{m}^{-1}$ to compute the equivalent width of the emission line ($-0.96 \pm 0.02 \text{ \AA}$), line flux ($1.20 \pm 0.04 \times 10^{-17} \text{ W m}^{-2}$), and line luminosity ($\log(L_{\text{Pa}\beta}/L_\odot) = -5.11 \pm 0.09 \text{ dex}$). The corresponding accretion luminosity is $\log(L_{\text{acc}}/L_\odot) = -2.9 \pm 1.0 \text{ dex}$ using the empirical correlation between accretion luminosity and $\text{Pa}\beta$ line luminosity from Natta et al. (2004). We find a mass accretion rate of $\log(\dot{M}) = -9.4 \pm 1.1 M_\odot \text{ yr}^{-1}$ using $\dot{M} = 2L_{\text{acc}}R_*/(GM_*)$, where G is the gravitational constant and M_* is the stellar mass. We adopt a stellar radius, R_* , of $1.1 \pm 0.2 R_\odot$ based on the age and luminosity of the system and evolutionary models (Allard et al. 2012) and a stellar mass of $0.20^{+1.0}_{-0.05} M_\odot$ (Section 3.4).

For 2M0441+2301 Ab, we use the $\pm 0.01 \mu\text{m}$ region adjacent to the $\text{Pa}\beta$ line to define the pseudocontinuum level and measure a $\text{Pa}\beta$ equivalent width of $-0.84 \pm 0.11 \text{ \AA}$. This corresponds to a line flux of $6.7 \pm 0.9 \times 10^{-19} \text{ W m}^{-2}$, a line luminosity of $\log(L_{\text{Pa}\beta}/L_\odot) = -6.4 \pm 0.1 \text{ dex}$, an accretion luminosity of $\log(L_{\text{acc}}/L_\odot) = -4.7 \pm 1.3 \text{ dex}$, and a mass accretion rate of $\log(\dot{M}) = -10.8 \pm 1.3 M_\odot \text{ yr}^{-1}$ assuming a radius of $0.41 \pm 0.02 R_*$ (Baraffe et al. 2003) and a mass of $35 \pm 5 M_{\text{Jup}}$ (Section 3.4).

3.3. Atmospheric Model Fitting

Atmospheric models can be used to infer the physical properties of the 2M0441+2301AabBab system such as the components’ effective temperatures (T_{eff}) and surface gravities ($\log g$) by fitting synthetic spectra to our OSIRIS observations. We first fit the BT-Settl models (Allard et al. 2012) with “CIFIST2011” solar abundances (Caffau et al. 2010) to individual J , H , and K spectral

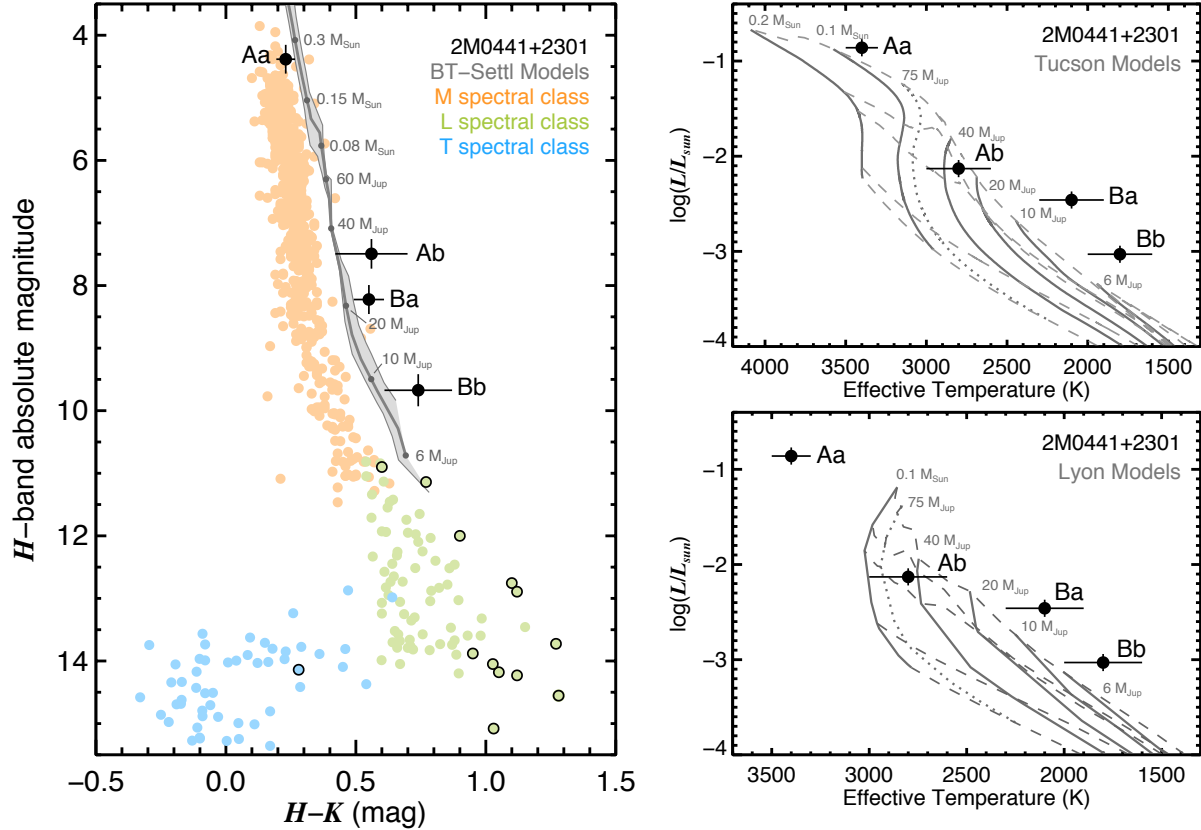


FIG. 4.— Comparison of 2M0441+2301 AabBab with theoretical isochrones. *Left*: The BT-Settl models (Baraffe et al. 2015) spanning 1, 2, and 3 Myr isochrones from right to left are consistent within 1σ with 2M0441+2301 AabBab in the M_H versus $H-K$ near-infrared color-magnitude diagram. All photometry has been converted to the MKO filter system. Comparison low-mass field objects are from the literature (Dupuy & Liu 2012), and symbols with dark borders represent young brown dwarfs and giant planets as opposed to old stars and brown dwarfs. *Top Right*: The 1 Myr isochrones from the Tucson models (Burrows et al. 1997) are generally consistent with the empirical isochrone traced by this quadruple system at the 2σ level, though the Ba and Bb components are cooler than expected from these models by 200–300 K. 1 Myr, 5 Myr, 10 Myr, 100 Myr, and 1 Gyr isochrones are plotted. *Bottom Right*: Same as the top right panel, but for the Lyon (Cond) evolutionary models (Baraffe et al. 2003). These models extend to $0.1 M_\odot$ and are consistent with 2M0441+2301 Ab, Ba, and Bb at the 2σ level. 1 Myr, 5 Myr, 10 Myr, 100 Myr, and 1 Gyr isochrones are plotted.

regions and to the entire flux-calibrated $1.2\text{--}2.4\ \mu\text{m}$ spectrum of all components in the system. The grid spans 1100 K to 4000 K in T_{eff} ($\Delta T_{\text{eff}} = 100\ \text{K}$) and 2.5 dex to 5.5 dex in $\log g$ ($\Delta \log g = 0.5\ \text{dex}$ [cgs units]). For each synthetic spectrum, we compute the scale factor that minimizes the χ^2 value between the model and the data. This also gives the objects radius R since the scale factor is simply R^2/d^2 , where d is the distance to the object. We adopt the characteristic distance to Taurus of $145 \pm 15\ \text{pc}$ throughout this work. The models qualitatively reproduce our near-infrared spectra with various combinations of temperature and gravity, but the best-fit values to different bandpasses are generally not self-consistent and are therefore unreliable, yielding unphysical values that differ by up to 1300 K and 2.0 dex for the same object. This is likely a result of missing opacity sources, incomplete atomic and molecular line lists, and imperfect cloud prescriptions in the models. For example, although fits to the individual bandpasses of 2M0441+2301 Bb provide good reduced chi-squared values, the model effective temperatures range from 1600 K to 2500 K and the inferred radii span 1.6 to $5.4 R_{\text{Jup}}$.

An alternative approach is to use photometry to constrain the components’ effective temperatures since this

spans a broader range of wavelengths and is less sensitive to the detailed physics and input line lists compared to our near-infrared spectra. After flux calibrating the models to the H -band monochromatic flux density, we identify the best matches to the available photometry of all four objects spanning $0.4\text{--}3\ \mu\text{m}$. As with comparisons to our spectra, the best-fitting models often have unphysical surface gravities. We therefore fix the surface gravities to the predicted values from the Baraffe et al. (2003) evolutionary models because gravity is only minimally influenced by model assumptions. We adopt values of $\log g = 4.0\ \text{dex}$ for Aa and $\log g = 3.5\ \text{dex}$ for Ab, Ba, and Bb and compute χ^2 values for a range of effective temperatures (1500 K to 4000 K). The best matches have effective temperatures of 3400 K for Aa, 2800 K for Ab, 2100 K for Ba, and 1800 K for Bb.

The results for Ba and Bb are up to 500 K cooler than recent spectral type-effective temperature calibrations for young stars from Herczeg & Hillenbrand (2014), which are derived by fitting the same grid of BT-Settl atmospheric models we use in this work to optical spectra of T Tauri stars. This discrepancy may reflect the paucity of photometric observations for 2M0441+2301 Ab, Ba, and Bb shortward of J band where the SED

turns over and provides the best constraint on T_{eff} . The reduced χ^2 values (χ^2_{ν}) are much larger than unity ($\chi^2_{\nu} \sim 10$ to 300), implying the photometric uncertainties are underestimated and/or there are systematic errors in the models. Since these data do not appear to be standard deviates of the models, maximum likelihood methods for establishing parameter confidence regions like constant $\Delta\chi^2$ boundaries about the minimum χ^2 values are not valid here. We therefore adopt a single grid step (100 K) as an estimate of the uncertainty in T_{eff} for Aa and two grid steps (200 K) for the substellar objects. Note that we have assumed zero reddening for these fits, but reddening up to $A_V = 0.5$ mag does not change the fitting results by more than 1σ . Additional resolved optical photometry would provide better constraints on T_{eff} and $\log g$, which in turn would enable more rigorous tests of substellar evolutionary models.

3.4. Luminosities and Masses

Integrating the models and adopting the mean Taurus distance gives luminosities of $\log(L/L_{\odot}) = -0.86 \pm 0.09$ dex, -2.13 ± 0.09 dex, -2.46 ± 0.09 dex, and -3.03 ± 0.09 dex for Aa, Ab, Ba, and Bb, respectively. Assuming a uniform likelihood of ages between 1 to 3 Myr, the corresponding masses of the substellar components are $35 \pm 5 M_{\text{Jup}}$ for Ab, $19 \pm 3 M_{\text{Jup}}$ for Ba, and $9.8 \pm 1.8 M_{\text{Jup}}$ for Bb from interpolated substellar evolutionary models (Baraffe et al. 2003). We adopt a mass of $0.20^{+1.0}_{-0.05} M_{\odot}$ for the primary star Aa based on recent low mass stellar evolutionary models (Baraffe et al. 2015). The mass we find for Bb is somewhat greater than Todorov et al. (2010) owing to our slightly higher luminosity measurement and broader assumed age range of 1 to 3 Myr.

Altogether this confirms that 2M0441+2301 Bb is similar in mass and separation to directly imaged planets like HR 8799 bcde (Marois et al. 2008; Marois et al. 2010) and β Pic b (Lagrange et al. 2010). The mass ratios of these systems, however, differ by nearly two orders of magnitude; the HR 8799 and β Pic systems have mass ratios of about 150–220, but for the 2M0441+2301 Bab binary it is only about 1.9. Together with environmental clues such as apparently coplanar multiple planets and an unusually massive and extended debris disk, the high mass ratios of HR 8799 and β Pic point to an alternative formation route compared with 2M0441+2301 Bab (see Section 4). Finally, these results also confirm that 2M0441+2301 AabBab is the lowest-mass quadruple system currently known, with a total mass of about $0.26 M_{\odot}$.

4. DISCUSSION

As a coeval and presumably chemical homogeneous quadruple system spanning the stellar to planetary mass regimes, 2M0441+2301 AabBab also provides a unique opportunity to test pre-main sequence and giant planet evolutionary models similar to other high-order stellar/substellar multiple systems in Taurus like GG Tau (White & Ghez 2001). Figure 4 shows the location of 2M0441+2301 AabBab in color-magnitude and Hertzsprung-Russell diagrams. Evolutionary model isochrones spanning 1 to 3 Myr are broadly consistent with the data at the 1 to 2σ levels.

We detect orbital motion for the first time in both the Aab and Bab binaries. 2M0441+2301Aab has undergone

significant changes in separation of 1.4 ± 0.2 mas yr^{-1} and in position angle (P.A.) of $-1.3 \pm 0.02^{\circ}$ yr^{-1} since 2008 (Kraus et al. 2011; Todorov et al. 2010; Todorov et al. 2014). 2M0441+2301 Bab is moving by -1.5 ± 0.5 mas yr^{-1} in separation and $2.0 \pm 0.3^{\circ}$ yr^{-1} in P.A. Unfortunately, the long orbital periods of about 300–400 years for each subsystem means that dynamical mass measurements will not be possible for at least several decades.

The wide separation between 2M0441+2301 Aab and Bab, the hierarchical orbital architecture of the system, and the low mass ratios of the Ab, Ba, and Bb components relative to the primary star Aa argue against formation by core accretion or stellar capture. Simulations of fragmenting disks can result in close substellar companions and ejected brown dwarf-planetary mass object binaries, but such low mass quadruple systems with a near ejection of one pair is difficult to reproduce with this formation channel (Li et al. 2015). Instead, the 2+2 hierarchy of 2M0441+2301 AabBab resembles the configuration of the most common stellar quadruples, which outnumber 3+1 hierarchies in planetary-like configurations by at least 4 to 1 among Sun-like stars within 25 pc (Tokovinin 2014). High order multiple systems like 2M0441+2301 AabBab provide important clues about the masses, critical densities, characteristic sizes, and opacity limits of fragmenting molecular cloud cores. This is particularly true at young ages and in low density star forming regions before significant dynamical unfolding has occurred and where interactions with nearby stars are minimal (Reipurth & Mikkola 2015; Pineda et al. 2015). Although the details and universality of quadruple star formation remain unclear, one possible formation route for this system is through two primary fragmentation events which each subsequently underwent a secondary fragmentation following H_2 dissociation, resulting in two short-period binaries on weakly bound orbits about each other (Whitworth & Stamatellos 2006). If the current separation of at least 1800 AU reflects the nascent architecture of the system, then the binary pairs have undergone fewer than 20 full orbits around each other in 3 Myr.

The lower limit of cloud fragmentation has been extensively explored with increasingly sophisticated simulations of collapsing turbulent molecular clouds (Bate 2009). Opacity-limited fragments between about 3 to $10 M_{\text{Jup}}$ can be produced if accretion is rapidly halted through dynamical encounters or ejections out of dense cloud cores (Padoan & Nordlund 2004). This is generally consistent with empirical determinations of the initial mass function, which show a smooth and continuous distribution down to 5 to $10 M_{\text{Jup}}$ and suggest a common origin with most stars and brown dwarfs (Chabrier 2003). This mass range also coincides with the lowest-mass companions imaged around stars and brown dwarfs (Brandt et al. 2014). However, the formation pathway of individual systems is often ambiguous since free-floating planetary-mass objects could represent ejections from planet-planet scattering events, and directly imaged planets could be scattered or in situ products of disk instability or core accretion. Confirming the low mass of 2M0441+2301 Bb demonstrates that fragmenting molecular clouds can create companions which overlap in mass with bona fide planets formed in disks, implying that

some of the directly imaged planets orbiting stars and brown dwarfs may represent the tail end of turbulent fragmentation rather than the tip of the iceberg of planet formation.

We thank K. Deck for helpful suggestions for improving this article, M. Brown for contributing telescope time for our NIRC2 observations, and the entire Keck Observatory staff for their exceptional support. We utilized data products from the Two Micron All Sky Survey, which is a joint project of the University of Massachusetts and the Infrared Processing and Analysis Center/California Institute of Technology,

funded by the National Aeronautics and Space Administration and the National Science Foundation. NASA's Astrophysics Data System Bibliographic Services together with the VizieR catalogue access tool and SIMBAD database operated at CDS, Strasbourg, France, were invaluable resources for this work. This research has benefitted from the SpeX Prism Spectral Libraries, maintained by Adam Burgasser at <http://pono.ucsd.edu/~adam/browndwarfs/spexprism>. Finally, mahalo nui loa to the kama'āina of Hawai'i for their support of Keck and the Mauna Kea observatories. We are grateful to conduct observations from this mountain.

Facilities: Keck:II (NIRC2), Keck:II (OSIRIS)

REFERENCES

- Adame, L., et al. 2010, *The Astrophysical Journal*, 726, L3
 Allard, F., Homeier, D., & Freytag, B. 2012, *Philosophical Transactions of the Royal Society A: Mathematical, Physical and Engineering Sciences*, 370, 2765
 Allers, K. N., & Liu, M. C. 2013, *The Astrophysical Journal*, 772, 79
 Baraffe, I., Chabrier, G., Barman, T. S., Allard, F., & Hauschildt, P. H. 2003, *A&A*, 402, 701
 Baraffe, I., Homeier, D., Allard, F., & Chabrier, G. 2015, arXiv
 Barman, T. S., Macintosh, B., Konopacky, Q. M., & Marois, C. 2011, *The Astrophysical Journal*, 733, 65
 Bate, M. R. 2009, *Monthly Notices RAS*, 392, 590
 Boss, A. P. 1997, *Science*, 276, 1836
 Bowler, B. P., Liu, M. C., Kraus, A. L., & Mann, A. W. 2014, *ApJ*, 784, 65
 Brandt, T. D., et al. 2014, *ApJ*, 794, 159
 Bulger, J., Patience, J., Ward-Duong, K., Pinte, C., Bouy, H., Menard, F., & Monin, J.-L. 2014, *A&A*, 570, A29
 Burgasser, A. J. 2014, arXiv
 Burrows, A., et al. 1997, *Astrophysical Journal*, 491, 856
 Caffau, E., Ludwig, H. G., Steffen, M., Freytag, B., & Bonifacio, P. 2010, *Sol Phys*, 268, 255
 Chabrier, G. 2003, *The Publications of the Astronomical Society of the Pacific*, 115, 763
 Cushing, M. C., Vacca, W. D., & Rayner, J. T. 2004, *PASP*, 116, 362
 Davies, M. B., Adams, F. C., Armitage, P., Chambers, J., Ford, E., Morbidelli, A., Raymond, S. N., & Veras, D. 2013, arXiv
 Dupuy, T. J., & Liu, M. C. 2012, *The Astrophysical Journal Supplement*, 201, 19
 Herczeg, G. J., & Hillenbrand, L. A. 2014, *ApJ*, 786, 97
 Kraus, A. L., Ireland, M. J., cieza, L. A., hinkley, S., Dupuy, T. J., Bowler, B. P., & Liu, M. C. 2014, *ApJ*, 781, 20
 Kraus, A. L., Ireland, M. J., Martinache, F., & Hillenbrand, L. A. 2011, *The Astrophysical Journal*, 731, 8
 Lagrange, A.-M., et al. 2010, *Science*, 329, 57
 Lambrechts, M., & Johansen, A. 2012, *A&A*, 544, A32
 Larkin, J., et al. 2006, *Proc. SPIE*, 6269, 42
 Li, Y., Kouwenhoven, M. B. N., Stamatellos, D., & Goodwin, S. P. 2015, *ApJ*, 805, 1
 Liu, M. C., Dupuy, T. J., & Leggett, S. K. 2010, *The Astrophysical Journal*, 722, 311
 Low, C., & Lynden-Bell, D. 1976, *Royal Astronomical Society*, 176, 367
 Luhman, K. L., Mamajek, E. E., Allen, P. R., & Cruz, K. L. 2009, *The Astrophysical Journal*, 703, 399
 Markwardt, C. B. 2009, *Astronomical Data Analysis Software and Systems XVIII ASP Conference Series*, 411, 251
 Marley, M. S., Saumon, D., Cushing, M., Ackerman, A. S., Fortney, J. J., & Freedman, R. 2012, *The Astrophysical Journal*, 754, 135
 Marois, C., Macintosh, B., Barman, T., Zuckerman, B., Song, I., Patience, J., Lafreniere, D., & Doyon, R. 2008, *Science*, 322, 1348
 Marois, C., Zuckerman, B., Konopacky, Q. M., Macintosh, B., & Barman, T. 2010, *Nature*, 468, 1080
 Mieda, E., et al. 2014, *PASP*, 126, 250
 Natta, A., Testi, L., Muzerolle, J., Randich, S., Comer N, F., & Persi, P. 2004, *A&A*, 424, 603
 Padoan, P., & Nordlund, Å. 2004, *The Astrophysical Journal*, 617, 559
 Pineda, J. E., et al. 2015, *Nature*, 518, 213
 Pollack, J. B., Hubickyj, O., Bodenheimer, P., Lissauer, J. J., Podolak, M., & Greenzweig, Y. 1996, *Icarus*, 124, 62
 Rayner, J. T., Cushing, M. C., & Vacca, W. D. 2009, *The Astrophysical Journal Supplement*, 185, 289
 Reipurth, B., & Mikkola, S. 2015, *The Astronomical Journal*, 149, 1
 Stamatellos, D., & Whitworth, A. P. 2009, *Monthly Notices RAS*, 392, 413
 Todorov, K., Luhman, K. L., & Mcleod, K. K. 2010, *The Astrophysical Journal*, 714, L84
 Todorov, K. O., Luhman, K. L., Konopacky, Q. M., Mcleod, K. K., Apai, D., Ghez, A. M., Pascucci, I., & Robberto, M. 2014, *ApJ*, 788, 40
 Tokovinin, A. 2014, *The Astronomical Journal*, 147, 87
 Vacca, W. D., Cushing, M. C., & Rayner, J. T. 2003, *PASP*, 115, 389
 van Dam, M. A., et al. 2006, *Publications of the Astronomical Society of the Pacific*, 118, 310
 White, R. J., & Ghez, A. M. 2001, *The Astrophysical Journal*, 556, 265
 Whitworth, A. P., & Stamatellos, D. 2006, *A&A*, 458, 817
 Wizinowich, P. L., et al. 2006, *The Publications of the Astronomical Society of the Pacific*, 118, 297
 Wu, Y.-L., et al. 2015, *ApJ*, 801, 4
 Yelda, S., Lu, J. R., Ghez, A. M., Clarkson, W., Anderson, J., Do, T., & Matthews, K. 2010, *The Astrophysical Journal*, 725, 331

TABLE 1
RELATIVE PHOTOMETRY AND ASTROMETRY

Name	UT Date	Inst.	$N \times \text{Exp.}$ Time (s)	Filt.	Sep. ($''$)	P.A. ($^\circ$)	Δmag	m_A (mag)	m_B mag	FWHM (mas)
2M0441Aab	2014 Nov 10	NIRC2	7×15	<i>Y</i>	230 ± 2	79.3 ± 0.6	3.16 ± 0.16	11.37 ± 0.02	14.53 ± 0.15	96 ± 29
2M0441Aab	2014 Nov 10	NIRC2	11×5	<i>J</i>	234 ± 2	79.4 ± 0.6	2.96 ± 0.06	10.77 ± 0.04	13.73 ± 0.07	65 ± 12
2M0441Aab	2014 Nov 10	NIRC2	7×5	<i>H</i>	233.0 ± 1.6	79.9 ± 0.2	3.11 ± 0.07	10.19 ± 0.03	13.30 ± 0.07	65 ± 17
2M0441Aab	2014 Nov 10	NIRC2	6×5	<i>K_S</i>	232.0 ± 1.3	79.1 ± 0.3	2.77 ± 0.13	9.94 ± 0.02	12.71 ± 0.12	64 ± 5
2M0441Aab	2014 Dec 08	OSIRIS	8×300	<i>Jbb</i>	3.3 ± 0.3	10.70 ± 0.05	14.0 ± 0.3	54 ± 5
2M0441Aab	2014 Dec 08	OSIRIS	6×300	<i>Hbb</i>	3.14 ± 0.18	10.20 ± 0.03	13.34 ± 0.17	58 ± 3
2M0441Aab	2014 Dec 08	OSIRIS	6×300	<i>Kbb</i>	2.81 ± 0.10	9.96 ± 0.02	12.77 ± 0.10	54 ± 1
2M0441Bab	2014 Nov 10	NIRC2	7×60	<i>H</i>	93 ± 2	132.6 ± 1.1	1.45 ± 0.14	14.03 ± 0.05	15.48 ± 0.12	88 ± 10
2M0441Bab	2014 Nov 10	NIRC2	7×30	<i>K_S</i>	97.5 ± 1.0	132.0 ± 0.6	1.24 ± 0.05	13.46 ± 0.03	14.70 ± 0.05	65 ± 4
2M0441Bab	2014 Dec 08	OSIRIS	10×400	<i>Jbb</i>	1.7 ± 0.2	14.57 ± 0.06	16.26 ± 0.17	67 ± 7
2M0441Bab	2014 Dec 08	OSIRIS	8×300	<i>Hbb</i>	1.42 ± 0.19	14.06 ± 0.05	15.47 ± 0.15	88 ± 9
2M0441Bab	2014 Dec 08	OSIRIS	8×300	<i>Kbb</i>	1.35 ± 0.17	13.50 ± 0.05	14.85 ± 0.14	79 ± 10